
Article:
Ma, X.Y., Li, G. orcid.org/0000-0002-5956-4033, Jewell, G.W. et al. (1 more author) (2018) Quantitative analysis of contribution of airgap field harmonics to torque production in 3-phase 12-slot/8-pole doubly-salient synchronous reluctance machines. IEEE Transactions on Magnetics, 54 (9). 8104611. ISSN 0018-9464

https://doi.org/10.1109/TMAG.2018.2848236

Quantitative Analysis of Contribution of Airgap Field Harmonics to Torque Production in 3-Phase 12-Slot/8-pole Doubly-Salient Synchronous Reluctance Machines

X. Y. Ma, G. J. Li, *Senior Member*, *IEEE*, G. W. Jewell, and Z. Q. Zhu, *Fellow*, *IEEE*
Department of Electronic & Electrical Engineering, the University of Sheffield, Sheffield, UK
g.li@sheffield.ac.uk

***Abstract*—This paper adopts simple analytical modelling to investigate the contribution of airgap field harmonics to the torque production in some 3-phase, 12-slot/8-pole doubly-salient synchronous reluctance machines (DSRMs) with both conventional and mutually-coupled winding configurations. The airgap flux density has been calculated based on the analytically obtained magnetomotive force and doubly-salient airgap permeance for both the double layer and single layer DSRMs with different winding configurations. Then the contribution of different airgap field harmonics to average torque and torque ripple can be investigated and validated by direct finite element analyses. It has been found that in the DSRM, the 10^{th} order harmonic in the double layer conventional (DLC), the 4^{th} order harmonic in the double layer mutually-coupled (DLMC), the 7^{th} order harmonic in the single layer conventional (SLC) and the 10^{th} order harmonic in the single layer mutually-coupled (SLMC) have the highest contribution to positive average torque while with positive influence on torque ripple reduction. However, the 2^{nd} order harmonic in the DLC, the 8^{th} order harmonic in the DLMC, the 5^{th} order harmonic in the SLC and the 2^{nd} order harmonic in the SLMC machines mainly reduce the average torque.**

***Index Terms*—Airgap field, analytical modelling, doubly salient synchronous reluctance machine, torque.**

I. Introduction

SWICTHED reluctance machines become increasingly attractive in various industry sectors like domestic appliances, renewable energy, electrical vehicles and hybrid electrical vehicles, etc. This is mainly due to the apparent merits such as no permanent magnets or field windings on the rotors, which lead to low cost, simple and robust machine structures, etc. [1] [2] [3] [4]. However, the switched reluctance machines exhibit higher levels of vibrations and acoustic noise when compared to permanent magnet machines and induction machines [5] [6]. This is mainly due to their doubly salient structures, which can cause abrupt changes in radial force around the airgap. In addition, the abrupt change in phase current due to the conventional square wave unipolar phase current supply is another factor for higher vibration and acoustic noise. In addition, with the conventional square wave unipolar excitation, special power-converter is often used for conventional switched reluctance machines and it to some extent limits the foothold of such machines in the market. In contrast, with similar magnet-free structures, the synchronous reluctance machines can employ the off-the-shelf 3-phase bridge inverters with sinewave excitation, which are also used in synchronous and induction machines [7] [8]. However, most synchronous reluctance machines have complicated non-salient rotor structures with flux barriers inside the rotor iron core which increases the difficulty and cost in manufacturing. In order to employ the doubly-salient machine structure for simpler manufacturing and to use the standard 3-phase inverter for reducing the system cost, the SRMs can also adopt the sinewave excitation which are in effect doubly-salient synchronous reluctance machines (DSRMs).

Similar to switched reluctance machines, both the concentrated and distributed winding can be applied for DSRMs, which have significant influence on the electromagnetic performances. It is well-established that switched reluctance machine with double layer conventional winding configuration obtains its best electromagnetic performance when it adopts the conventional square wave unipolar current with 120 elec. deg. conduction [9]. However, the DSRM with double layer conventional winding (DLC) cannot have a good performance with sinewave excitation since only self-inductances can contribute to the electromagnetic torque. Different from the DLC, the machine with double layer mutually-coupled winding (DLMC) can have both self- and mutual-inductances since the flux in one phase also links to other phases [9] [10] [11]. In addition, the DLMC is less sensitive to magnetic saturation due to the less concentrated magnetomotive force (MMF) in the stator iron core. As a result, it has been found that the DLMC can achieve better overload torque capability [7]. Moreover, it is evident in [7] [12] that the vibration and acoustic noise can be reduced with the DLMC. However, the torque ripple of this machine is higher than that with DLC due to the nature of its self- and mutual-inductances.

With sinewave excitation, higher average torque with lower torque ripple can be achieved by both single layer conventional (SLC) and single layer mutually-coupled (SLMC) machines at low current levels, in which the winding configurations are similar to their double layer counterparts [13]. However, similar to the single layer winding structure in the well-established fully-pitched winding machine, the two single layer machines are more sensitive to magnetic saturation, making them less attractive at high phase current than the double layer machines.

In this paper, in order to investigate the torque production mechanism between different winding configurations, both the double or single layer machines have been selected for quantitative analysis of the airgap field harmonics and their contribution to the torque performances (average torque and torque ripple). Some simple analytical torque models have been developed based on the airgap permeance and armature winding MMFs. In order to evaluate the slotting effect on the airgap permeance and hence on the airgap field,

two main methods can be adopted, which have been well established in literature. One is to evaluate a relative permenace function on the basis of the conformal transformation (considered in this paper), the other approach is to use the subdomain models, which might be relatively more accurate, but more complicated to use as well [14] [15] [16] [17]. In addition, the analytical models of the airgap flux density have been developed according to the MMF-permeance theory reported in [18] [19] [20] [21]. It is worth mentioning that in order to simplify the analyses, the permeability of the stator and the rotor iron cores has been assumed to be infinite. As a result, the magnetic saturation is not considered. In addition, the analytical model will be 2D, and hence the end effect is neglected as well.

II. Influence of Winding Configuration on MMF

A. Winding Configurations of Double Layer and Single Layer Machines

In this paper, the 3-phase 12-slot/8-pole DSRMs employ both the double/single layer, conventional/mutually-coupled winding configurations. To simplify the analysis, all the machines have the same dimensions and their design parameters are shown in TABLE I. The winding configurations and flux distributions of the double layer conventional and mutually-coupled (DLC and DLMC) are shown in Fig. 1 (a) and (b), respectively.

TABLE I MACHINE DIMENSIONS AND DESIGN PARAMETERS

Stator slot number	12	Active length (mm)	60
Rotor pole number	8	Stator slot opening coefficient β_s	0.49
Stator outer radius (mm)	45	Rotor slot opening coefficient β_r	0.57
Stator inner radius	29.3	Turn number per phase	132
Air gap length (mm)	0.5	Rated RMS current (A)	10
Rotor outer radius (mm)	28.8	Current density (A_{rms}/mm^2)	5.68
Rotor inner radius (mm)	9.3		

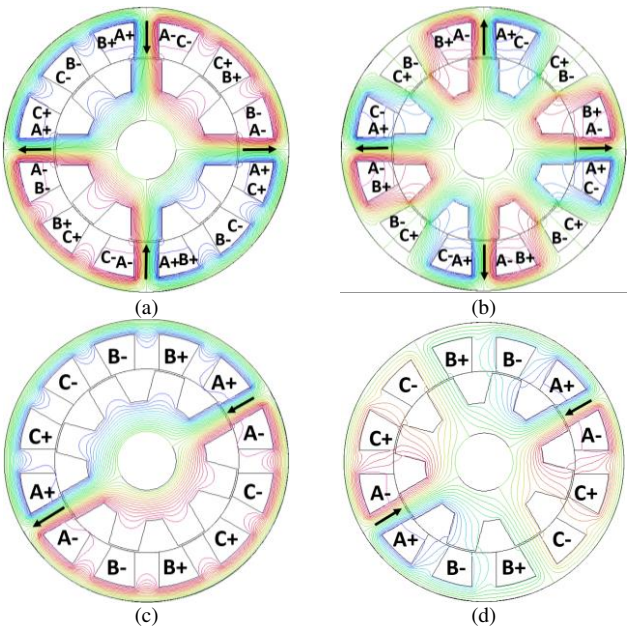

Fig. 1. Comparison of winding configurations and flux distributions between the 12-slot/8-pole DSRMs: (a) DLC, (b) DLMC, (c) SLC, and (d) SLMC. The rotor is at aligned position and phase A is supplied by a 10A dc current.

It can be found in Fig. 1 (a) that there is almost no mutual-flux in the DLC. However, the flux of phase A is also linked with other phases in the DLMC, as shown in Fig. 1(b). In addition, the number of flux paths of the phase A is doubled than that with the DLC. Also, the coil magnetic polarities of the phase A of the DLC is SNSN while it is SSSS for the DLMC. As a result, the MMF waveform of the phase A of the DLC should be different from that of the DLMC as will be detailed later on in this paper.

The flux distribution of their single layer counterparts: SLC and SLMC are shown in Fig. 1 (c) and (d), respectively, where the winding arrangements are similar to those in the double layer machines, but with single layer winding structures. Hence, the coil magnetic polarities are different as shown in TABLE II. It can be found that the DLC and DLMC have similar coil magnetic polarities as the SLC and SLMC, respectively. However, the periodicity of the magnetic polarities in the double layer machines is doubled than that in the single layer machines. Additionally, it is worth noting that the number of coils per phase of the double layer machines is doubled when compared to that of the single layer ones. However, the double layer machines have half number of turns per coil compared to the single layer ones, so they have the same number of turns per phase.

By way of example, with 4 coils per phase, the double layer machines have 33 turns per coil to achieve 132 series turns per phase. However, the single layer ones have 2 coils per phase and 66 turns per coil. Therefore, at the same current, the amplitude of single phase MMF of the single layer machines are doubled than that of the double layer ones, regardless of the winding configurations. This means that the single layer winding might generate more torque but it could be more prone to magnetic saturation as well.

TABLE II COIL MAGNETIC POLARITIES OF DSRMS WITH DIFFERENT WINDING CONFIGURATIONS

Winding configurations	Coil magnetic polarities
DLC	SNSNSNSNSNSN
DLMC	SSSSSSSSSSSS
SLC	NSNSNS
SLMC	NNNNNN

B. Analysis of Single-Phase MMF for Different Winding Configurations

According to the winding configurations and coil magnetic polarities, the single-phase MMF of both the double and single layer configurations can be calculated. It is worth noting that the waveform of the single-phase MMF of the double layer winding configurations are similar to their single layer counterpart, while their amplitudes (influenced by number of turns per coil) and periodicities (influenced by the periodicity of the coil magnetic polarities) are different. In order to avoid the duplication, only the DLC and DLMC have been selected for the MMF analytical modelling in this paper.

1) Conventional winding configurations

With 4 coils per phase, the coil magnetic polarities of the phase A of the DLC are SNSN. Therefore, the phase A winding has 2 pole pairs, and its MMF against angular position θ, at t=0, can be calculated over half of a mechanical period, i.e. $[0, \pi]$:

$$MMF_a(\theta, t=0) = \begin{cases} H & 0 \le \theta < \frac{1}{2}\theta_s - \frac{1}{2}\beta_s\theta_s \\ -\frac{2H}{\beta_s\theta_s}\left(\theta - \frac{1}{2}\theta_s\right) & \frac{1}{2}\theta_s - \frac{1}{2}\beta_s\theta_s \le \theta < \frac{1}{2}\theta_s \\ 0 & \frac{1}{2}\theta_s \le \theta < \frac{5}{2}\theta_s \\ -\frac{2H}{\beta_s\theta_s}\left(\theta - \frac{5}{2}\theta_s\right) & \frac{5}{2}\theta_s \le \theta < \frac{5}{2}\theta_s + \frac{1}{2}\beta_s\theta_s \\ -H & \frac{5}{2}\theta_s + \frac{1}{2}\beta_s\theta_s \le \theta < \frac{7}{2}\theta_s - \frac{1}{2}\beta_s\theta_s \\ \frac{2H}{\beta_s\theta_s}\left(\theta - \frac{7}{2}\theta_s\right) & \frac{7}{2}\theta_s - \frac{1}{2}\beta_s\theta_s \le \theta < \frac{7}{2}\theta_s \\ 0 & \frac{7}{2}\theta_s \le \theta < \frac{11}{2}\theta_s \\ \frac{2H}{\beta_s\theta_s}\left(\theta - \frac{11}{2}\theta_s\right) & \frac{11}{2}\theta_s \le \theta < \frac{11}{2}\theta_s + \frac{1}{2}\beta_s\theta_s \\ H & \frac{11}{2}\theta_s + \frac{1}{2}\beta_s\theta_s \le \theta < 6\theta_s \end{cases} \quad (1)$$

where $H = N_c I_{ph}$ is the MMF per coil ($N_c = 33$ for the double layer machines while $N_c = 66$ for the single layer machines). The dc phase current is used for the single-phase MMF modelling, while for the three-phase MMF modelling it is the phase peak current. θ_s is the stator pole pitch (30 mech. deg. for the 12-slot/8-pole machines), $\beta_s\theta_s$ is the stator slot opening which can be found in TABLE I, and θ is the angular position in mech. deg. Accordingly, (1) can be expanded into Fourier series over $[0, 2\pi]$ as

$$MMF_a(\theta, t=0) = \frac{2N_c I_{ph}}{\pi\beta_s\theta_s}\sum_{k=1}^{\infty}\frac{1}{k^2}C_{a,k}\cos(k\theta) \quad (2)$$

where the coefficient $C_{a,k}$ is shown in TABLE III. It can be found that the single-phase MMF of the DLC contains harmonic orders of 2, 6, 10, …, (4k-2), where k=1, 2, 3, … Accordingly, the magnitude of each harmonic in the single-phase MMF can be obtained.

TABLE III COEFFICIENT $C_{a,k}$ IN SINGLE-PHASE MMF OF DLC

$C_{a,k}$	n
$4\sin(\frac{1}{2}n\beta_s\theta_s) - 4\sqrt{3}\left[\cos\left(\frac{n\beta_s\theta_s}{2}\right) - 1\right]$	$2 + 24(k-1)$
$8\sin(\frac{1}{2}n\beta_s\theta_s)$	$6 + 24(k-1)$
$4\sin(\frac{1}{2}n\beta_s\theta_s) + 4\sqrt{3}\left[\cos\left(\frac{n\beta_s\theta_s}{2}\right) - 1\right]$	$10 + 24(k-1)$
$-4\sin(\frac{1}{2}n\beta_s\theta_s) + 4\sqrt{3}\left[\cos\left(\frac{n\beta_s\theta_s}{2}\right) - 1\right]$	$14 + 24(k-1)$
$-8\sin(\frac{1}{2}n\beta_s\theta_s)$	$18 + 24(k-1)$
$-4\sin(\frac{1}{2}n\beta_s\theta_s) - 4\sqrt{3}\left[\cos\left(\frac{n\beta_s\theta_s}{2}\right) - 1\right]$	$22 + 24(k-1)$

2) *Mutually-coupled winding configurations*

If the mutually-coupled winding is employed, the flux path is different from that of the DLC. It can be seen from Fig. 2 that the number of flux paths is doubled in the DLMC. In addition, its coil magnetic polarities, such as for the phase A, are SSSS. As a result, the periodicity of the single-phase MMF of the DLMC is 4 over one mechanical period ($[0, 2\pi]$), and the phase A MMF against the angular position θ, at t=0, is calculated over $\left[0, \frac{1}{2}\pi\right]$.

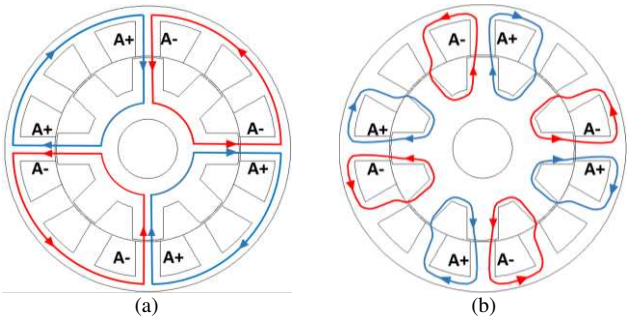

(a) (b)

Fig. 2. Flux paths in (a) double layer, and (b) single layer machines when the phase A is supplied.

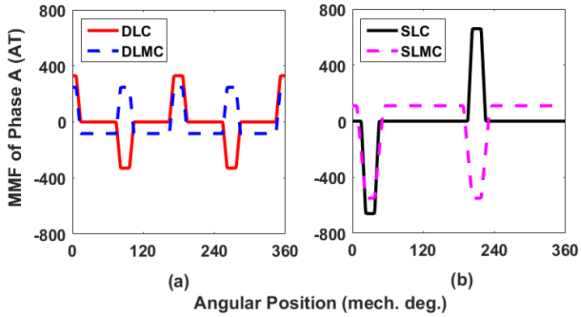

Fig. 3. Comparison of the single phase MMFs between the 12-slot/8-pole DSRMs. (a) double layer, and (b) single layer machines. Phase A is supplied with a 10A dc current.

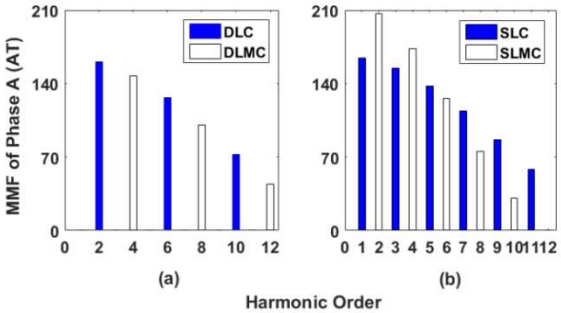

Fig. 4. Spectra of the single phase MMFs. (a) double layer, and (b) single layer machines. Phase A is supplied with a 10A dc current.

$$MMF_a(\theta, t=0) = \begin{cases} \frac{H}{2} - \delta_0 & 0 \le \theta < \frac{1}{2}\theta_s - \frac{1}{2}\beta_s\theta_s \\ -\frac{2H}{\beta_s\theta_s}\left(\theta - \frac{1}{2}\theta_s + \frac{1}{4}\beta_s\theta_s\right) - \delta_0 & \frac{1}{2}\theta_s - \frac{1}{2}\beta_s\theta_s \le \theta < \frac{1}{2}\theta_s \\ -\frac{H}{2} - \delta_0 & \frac{1}{2}\theta_s \le \theta < \frac{5}{2}\theta_s \\ \frac{2H}{\beta_s\theta_s}\left(\theta - \frac{5}{2}\theta_s - \frac{1}{4}\beta_s\theta_s\right) - \delta_0 & \frac{5}{2}\theta_s \le \theta < \frac{5}{2}\theta_s + \frac{1}{2}\beta_s\theta_s \\ \frac{H}{2} - \delta_0 & \frac{5}{2}\theta_s + \frac{1}{2}\beta_s\theta_s \le \theta < 3\theta_s \end{cases} \quad (3)$$

where

$$\delta_0 = \frac{1}{T}\int_0^{2\pi} MMF_a(\theta, \delta_0 = 0)d\theta = -\frac{H}{6}(\beta_s + 1) \quad (4)$$

δ_0 is referred to the dc component which is considered for the mutual flux path through other phases (when the phase A is excited). Accordingly, (3) can be expanded into Fourier series over $[0, 2\pi]$ as

$$MMF_a(\theta, t=0) = \frac{2N_c I_{ph}}{\pi\beta_s\theta_s}\sum_{k=1}^{\infty}\frac{1}{k^2}M_{a,k}\cos(k\theta) \quad (5)$$

where the coefficient $M_{a,k}$ is shown in TABLE IV. Therefore, the single-phase MMF of the DLMC contains harmonic orders of 4, 8, 12, …, (4k), where k=1, 2, 3, … It is apparent that the harmonic orders in MMF is different from the DLC due to different magnetic polarities.

TABLE IV COEFFICIENT $M_{a,k}$ IN SINGLE-PHASE MMF OF THE DLMC

$M_{a,k}$	n
$4\sqrt{3}\sin(\frac{1}{2}n\beta_s\theta_s)+4\left[\cos\left(\frac{n\beta_s\theta_s}{2}\right)-1\right]$	$4+24(k-1)$
$4\sqrt{3}\sin(\frac{1}{2}n\beta_s\theta_s)-4\left[\cos\left(\frac{n\beta_s\theta_s}{2}\right)-1\right]$	$8+24(k-1)$
$-8\left[\cos\left(\frac{n\beta_s\theta_s}{2}\right)-1\right]$	$12+24(k-1)$
$-4\sqrt{3}\sin(\frac{1}{2}n\beta_s\theta_s)-4\left[\cos\left(\frac{n\beta_s\theta_s}{2}\right)-1\right]$	$16+24(k-1)$
$-4\sqrt{3}\sin(\frac{1}{2}n\beta_s\theta_s)+4\left[\cos\left(\frac{n\beta_s\theta_s}{2}\right)-1\right]$	$20+24(k-1)$
$8\left[\cos\left(\frac{n\beta_s\theta_s}{2}\right)-1\right]$	$24+24(k-1)$

The single-phase MMFs of both the SLC and SLMC can be obtained in similar way, but they are not shown in this paper to save space. According to these Fourier series expressions, the single-phase MMFs of both the double and single layer machines are illustrated in Fig. 3 (a) and (b), respectively. Fig. 4 shows their spectra. It can be found that the MMF amplitudes of both the double layer DSRMs are lower than that of the single layer ones, but the periodicity is doubled. This is due to the doubled number of coils per phase but halved periodicity in the coil magnetic polarities, as mentioned previously. In addition, with the conventional winding configurations, the harmonic orders of the SLC are 2, 4, 6, …, (2k-1), where k=1, 2, 3, ..., while with the mutually-coupled winding configurations, the harmonic orders of the SLMC are 1, 3, 5, …, 2k, where k=1, 2, 3, ... Hence, the harmonic orders of the double layer DSRMs are doubled than those of the single layer ones, regardless of the winding configurations. Furthermore, it can be found that the phase A MMF is not zero at the angular position of other phases, e.g. 120 mech. deg., for phase B or C, in both the DLMC- and SLMCs. This is due to the mutual flux between phases as explained previously.

C. 3-Phase MMF Supplied with Sinewave Currents

Supplied with 3-phase sinewave currents as shown in (6), the 3-phase MMF can be calculated at different rotor positions.

$$\begin{cases} i_a = \sqrt{2}I_{rms}\sin(\omega t) \\ i_b = \sqrt{2}I_{rms}\sin(\omega t - \frac{2\pi}{3}) \\ i_c = \sqrt{2}I_{rms}\sin(\omega t + \frac{2\pi}{3}) \end{cases} \tag{6}$$

For the DLC, the 3-phase MMF is given by

$$MMF_{abc}(\theta,t) = \frac{3\sqrt{2}N_cI_{rms}}{\pi\beta_s\theta_s}\sum_{k=1}^{\infty}\frac{1}{k^2}C_{a,k}\sin\beta_C \tag{7}$$

where

$$\beta_C = \begin{cases} n\theta+\omega t & n=2+12(k-1) \\ 0 & n=6+12(k-1) \\ -n\theta+\omega t & n=10+12(k-1) \end{cases} \tag{8}$$

Similarly, the 3-phase MMF of the DLMC is given by

$$MMF_{abc}(\theta,t) = \frac{3\sqrt{2}N_cI_{rms}}{\pi\beta_s\theta_s}\sum_{k=1}^{\infty}\frac{1}{k^2}M_{a,k}\sin\beta_M \tag{9}$$

where

$$\beta_M = \begin{cases} -n\theta+\omega t & n=4+12(k-1) \\ n\theta+\omega t & n=8+12(k-1) \\ 0 & n=12+12(k-1) \end{cases} \tag{10}$$

It can be found from (8) to (10) that the 10th order harmonic of the DLC and the 4th order harmonic of the DLMC are forward rotating. However, the 2nd order harmonic of the DLC and the 8th order harmonic of the DLMC are backward rotating. Moreover, there are no triplen harmonics in the 3-phase MMF, as for other conventional 3-phase machines with neutral point. In addition, the rotation speed is determined by the rotor pole number but not by the stator winding pole numbers. Fig. 5 shows the comparison of the 3-phase MMFs at t=0 between the DSRMs with both the double and single layer windings and Fig. 6 shows their spectra.

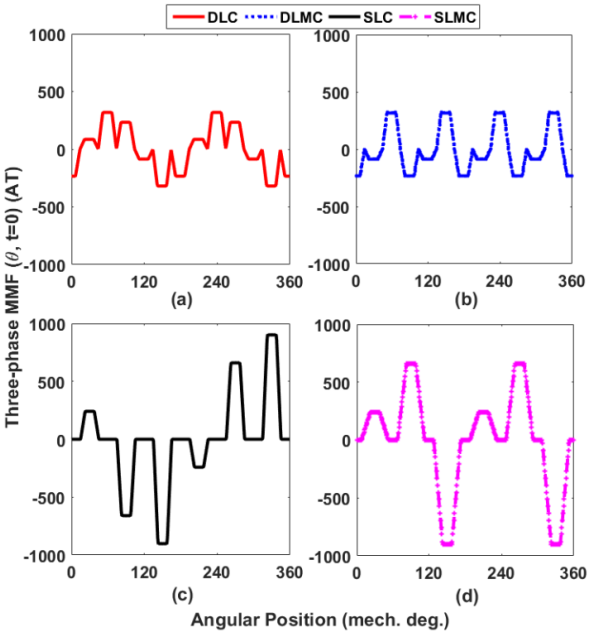

Fig. 5. Comparison of the 3-phase MMFs between the 12-slot/8-pole DSRMs at 10A_{rms}. (a) DLC, (b) DLMC, (c) SLC, and (d) SLMC.

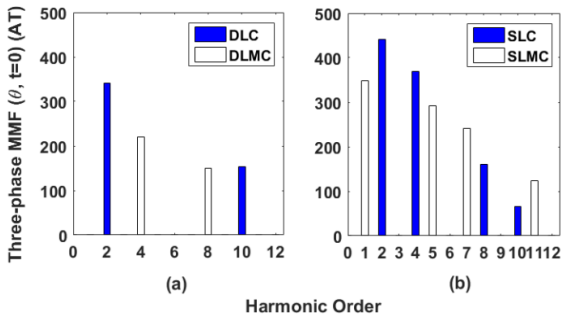

Fig. 6. Spectra of the 3-phase MMFs between the 12-slot/8-pole DSRMs at 10A_{rms}. (a) double layer, and (b) single layer machines.

III. Analysis of Airgap Flux Density

A. Airgap Permeance

In order to investigate the slotting effect on the air-gap flux density, the doubly slotted airgap is divided into three regions, e.g. the stator slots, the air-gap, and the rotor slots, as shown in Fig. 7. As a result, the resultant airgap permeance can be written by (11).

$$\Lambda_{resultant}(\theta,t)=\frac{1}{\delta_s(\theta)+\delta_r(\theta,t)+l_g} \tag{11}$$

where δ_s and δ_r are additional airgaps due to the stator and rotor slotting effect, respectively, and l_g is the airgap length. In addition, R_{s1} and R_{s2} are the radii of flux path lengths in the stator slot openings, and R_{r1} and R_{r2} are the radii of flux path lengths in the rotor slot openings. The resultant flux path in the stator and rotor slot openings have been derived in [20] and the additional airgap due to the stator and rotor slot openings over $[0,\theta_s]$ and $[0,\theta_r]$ are given by (12) and (13).

$$\delta_s(\theta)=\begin{cases}0 & 0\le\theta<\frac{1}{2}\theta_s-\frac{1}{2}\beta_s\theta_s\\ \frac{\pi R_{si}}{2}\frac{\sin(\frac{\theta}{2}-\frac{1}{4}\theta_s+\frac{\beta_s\theta_s}{4})\sin(\frac{\beta_s\theta_s}{4}-\frac{\theta}{2}+\frac{1}{4}\theta_s)}{\sin(\frac{\beta_s\theta_s}{4})\cos(\frac{\theta_s}{4}-\frac{\theta}{2})} & \frac{1}{2}\theta_s-\frac{1}{2}\beta_s\theta_s\le\theta<\frac{1}{2}\theta_s+\frac{1}{2}\beta_s\theta_s\\ 0 & \frac{1}{2}\theta_s+\frac{1}{2}\beta_s\theta_s\le\theta<\theta_s\end{cases} \tag{12}$$

$$\delta_r(\theta,t=0)=\begin{cases}0 & 0\le\theta<\frac{1}{2}\theta_r-\frac{1}{2}\beta_r\theta_r\\ \frac{\pi R_{ro}}{2}\frac{\sin(\frac{\theta}{2}-\frac{1}{4}\theta_r+\frac{\beta_r\theta_r}{4})\sin(\frac{\beta_r\theta_r}{4}-\frac{\theta}{2}+\frac{1}{4}\theta_r)}{\sin(\frac{\beta_r\theta_r}{4})\cos(\frac{\theta_r}{4}-\frac{\theta}{2})} & \frac{1}{2}\theta_r-\frac{1}{2}\beta_r\theta_r\le\theta<\frac{1}{2}\theta_r+\frac{1}{2}\beta_r\theta_r\\ 0 & \frac{1}{2}\theta_r+\frac{1}{2}\beta_r\theta_r\le\theta<\theta_r\end{cases} \tag{13}$$

where R_{si} is the stator inner radius and R_{ro} is the rotor outer radius. Expanding (12) and (13) using Fourier series analysis over $[0,2\pi]$ gives

$$\begin{aligned}\delta_s(\theta)=\frac{R_{si}(\pi\beta_s)^2}{72}+\sum_{k=1}^{+\infty}\Big\{&-\frac{R_{si}}{24k^2}\Big[1+\cos(2\pi k\beta_s)\\&-\frac{1}{\pi k\beta_s}\sin(2\pi k\beta_s)\Big]\Big\}\cos[6k(2\theta\\&-\theta_s+\beta_s\theta_s)]\\&+\sum_{k=1}^{+\infty}\Big\{\frac{R_{si}}{24k^2}\Big[\frac{1}{\pi k\beta_s}[1-\cos(2\pi k\beta_s)]\\&-\sin(2\pi k\beta_s)\Big]\Big\}\sin[6k(2\theta-\theta_s+\beta_s\theta_s)]\end{aligned} \tag{14}$$

$$\begin{aligned}\delta_r(\theta,t)=\frac{R_{ro}(\pi\beta_r)^2}{48}+\sum_{k=1}^{+\infty}\Big\{&-\frac{R_{ro}}{16k^2}\Big[1+\cos(2\pi k\beta_r)\\&-\frac{1}{\pi k\beta_r}\sin(2\pi k\beta_r)\Big]\Big\}\cos[4k(2\theta\\&-\theta_r+\beta_r\theta_r-2t)]\\&+\sum_{k=1}^{+\infty}\Big\{\frac{R_{ro}}{16k^2}\Big[\frac{1}{\pi k\beta_r}[1-\cos(2\pi k\beta_r)]\\&-\sin(2\pi k\beta_r)\Big]\Big\}\sin[4k(2\theta-\theta_r+\beta_r\theta_r\\&-2t)]\end{aligned} \tag{15}$$

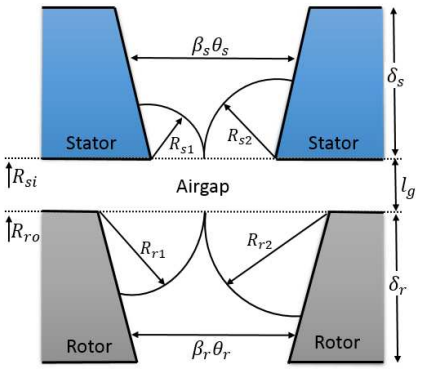

Fig. 7. Diagram for illustration of reciprocal of resultant airgap permeance with idealized flux path in slot openings.

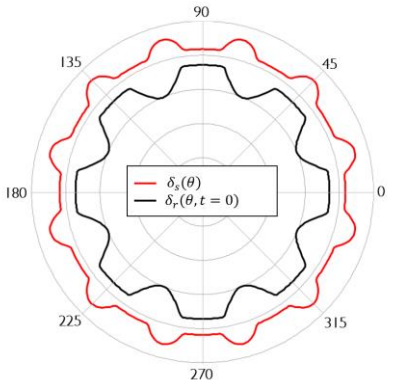

Fig. 8. Additional airgap δ due to stator and rotor slotting effect.

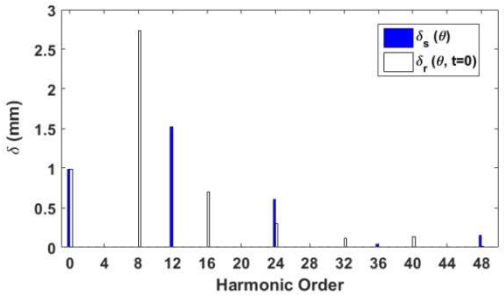

Fig. 9. Spectra of the additional airgap δ due to the stator and rotor slotting effect.

Accordingly, the additional airgaps due to the stator and rotor slotting effects and their spectra have been illustrated in Fig. 8 and Fig. 9, respectively. Besides the dc component (1mm), it is apparent that with a slot number of 12, the harmonic orders of the stator side airgap is 12k, where k=1, 2, 3, … Similarly, the harmonic orders of the rotor side airgap for a 8-pole machine is 8k. Substituting (14) and (15) into (11), the resultant airgap permeance can be obtained as

shown in Fig. 10. It can be found that the periodicity of the resultant airgap permeance in one mechanical period is 4, also, it is indeed the greatest common divisor of the slot and pole numbers. The harmonic orders of the resultant airgap permeance is $4k$ where k=1, 2, 3, …, as shown in Fig. 10 (b).

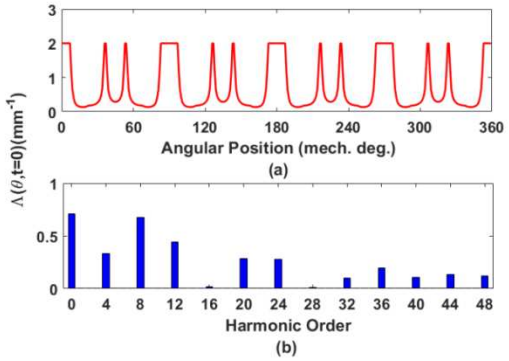

Fig. 10. Airgap permeance of the 12-slot/8-pole DSRMs. (a) airgap permeance $\Lambda\ (\theta, t = 0)$, and (b) spectra.

B. Airgap Flux Density

With the assumption of infinite permeability in the stator and rotor iron cores, the radial airgap flux density can be defined as

$$B_r\ (\theta, t) = \mu_0 MMF(\theta, t)\Lambda\ (\theta, t) \tag{16}$$

where μ_0 is the permeability of free space and Λ is the airgap permeance. It is worth mentioning that the analytical model of MMF in Section II only considers the excitation of the armature coils. Hence, only the stator scalar magnetic potential is defined but the rotor scalar magnetic potential is assumed to be zero. Indeed, this approach can be used for a non-salient rotor case. However, due to the doubly salient structure in the DSRMs, the MMF has to be modified in order to take the non-zero rotor scalar magnetic potential into account. According to Gauss's law for magnetism which states that $div\vec{B} = 0$, a coefficient q_c can be defined according to [20] as

$$q_c(t) = -\frac{\int_0^{2\pi} MMF_a(\theta)\Lambda\ (\theta, t)\ d\theta}{\int_0^{2\pi} \Lambda\ (\theta, t)\ d\theta} \tag{17}$$

Hence, the MMF can be modified by adding the coefficient q_c:

$$MMF_{modified,a}(\theta, t) = MMF_a(\theta, t) + q_c(t) \tag{18}$$

In addition, the coefficient q_c is calculated as zero for conventional winding machines, regardless of the single or double layer winding structures. This is because that their dc component of $MMF_a(\theta)\Lambda\ (\theta, t)$ equals zero, which is directly proportional to $\int_0^{2\pi} MMF_a(\theta)\Lambda\ (\theta, t)\ d\theta$. Hence, the MMF of the conventional DSRMs can still be calculated using the analytical modelling in section II. However, this is not the case for the mutually coupled DSRMs, as will be detailed in the following sections. Hence, it can be concluded that the coefficient q_c is only presented in the machine with mutually coupled winding configurations due to their unipolar MMF waveforms.

1) Single-phase airgap flux density

With the modified MMF, the airgap flux density can be obtained according to (16). The comparison of the single-phase airgap flux densities of the DLC- and DLMCs between 2D FEA and analytical modelling is shown in Fig. 11 (a) and (b), respectively. The phase A is supplied with a 10A dc current. Fig. 12 shows the spectra. It is apparent that the analytical results match well with the FE results for both the DLC and DLMCs. Due to the doubled effective rotor pole number, the DLMC presents doubled periodicity than that of the DLC in the single-phase airgap flux density. It can be found that the harmonic orders of the DLC are 2, 6, 10, …, (4k-2), while they are 4, 8, 12, …, 4k for the DLMC, where k=1, 2, 3, … Moreover, the harmonic orders of the single-phase airgap flux density is the same as that of the single-phase MMF which has been calculated in TABLE III and TABLE IV.

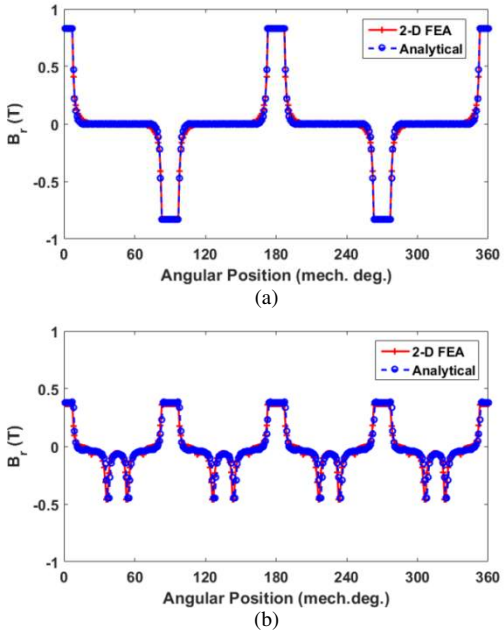

Fig. 11. Comparison of the single-phase airgap flux density B_r between 2D FEA and analytical modelling. Phase A is supplied with a 10A dc current. (a) DLC, and (b) DLMC.

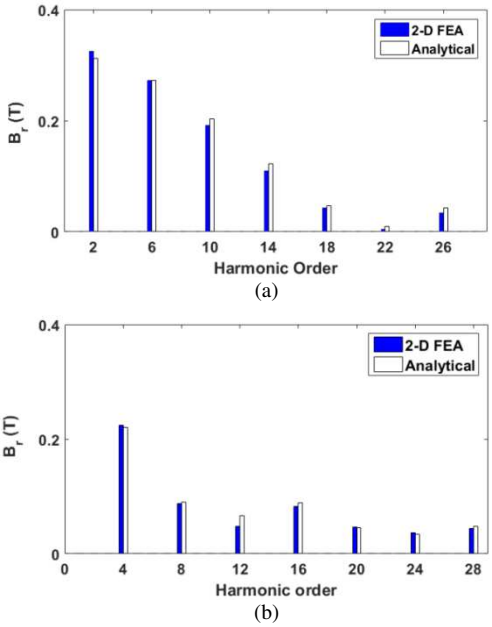

Fig. 12. Spectra of the single phase airgap flux density B_r between 2D FEA and analytical modelling. Phase A is supplied with a 10A dc current. (a) DLC, and (b) DLMC.

Similarly, the single-phase flux density of both the SLC and SLMCs can be obtained analytically and compared to 2D FEA as shown in Fig. 13, and the spectra are shown in Fig. 14. As mentioned previously, the periodicity of the MMF of both the single layer DSRMs is half of that of the double layer DSRMs. With the same airgap permenace, the periodicity of the airgap flux density of both the single layer DSRMs is also half of that of the double layer DSRMs. It is worth noting that the harmonic orders of the single-phase airgap flux density of the single layer DSRMs are half of those of the single layer DSRMs. For example, for the SLC, the harmonic orders are 1, 3, 5, …, (2k-1), while they are 2, 4, 6, …, 2k for the SLMC, where k=1, 2, 3, …

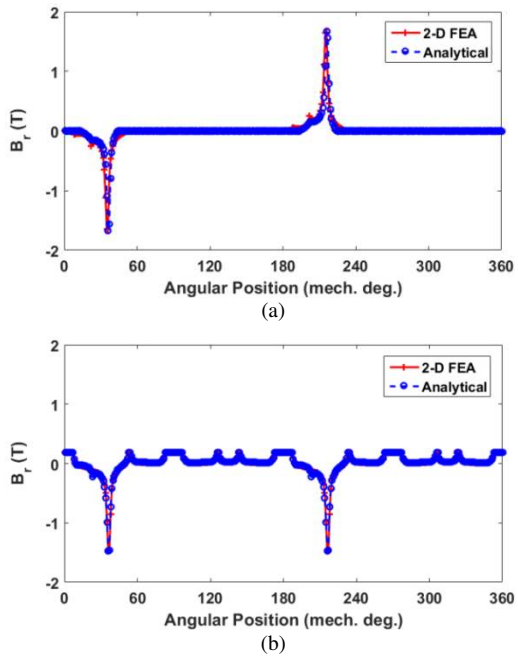

Fig. 13. Comparison of the single-phase airgap flux density B_r between 2D FEA and analytical modelling. Phase A is supplied with a 10A dc current. (a) SLC, and (b) SLMC.

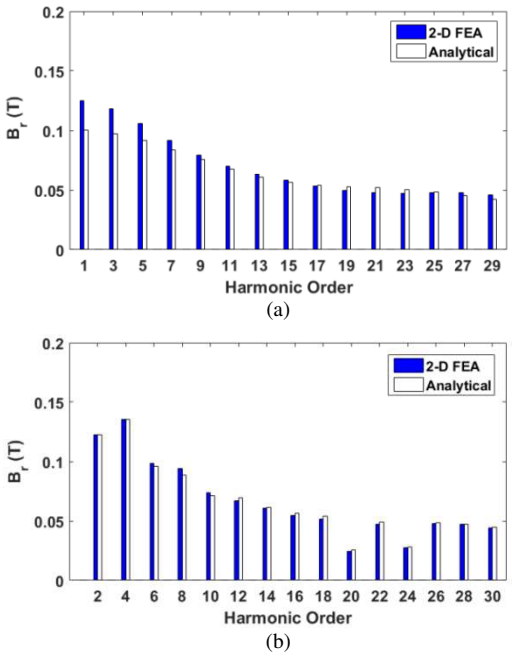

Fig. 14. Spectra of the single phase airgap flux density B_r between 2D FEA and analytical modelling. Phase A is supplied with a 10A dc current. (a) SLC, and (b) SLMC.

2) 3-phase airgap flux density

The 3-phase airgap flux density can be obtained by the same approach as for the single-phase airgap flux density. Fig. 15 and Fig. 16 compare the 2D FE and analytical 3-phase airgap flux densities and their spectra for the double layer DSRMs. The phase current is $10A_{rms}$. For completeness, the 3-phase airgap flux density and the spectra of the single layer DSRMs are shown in Fig. 17 and Fig. 18. It can be found that the 3-phase airgap flux densities have the same harmonic orders as the single-phase airgap flux density for both the double and single layer DSRMs. It is worth noting that the harmonics in the 3-phase airgap flux density contribute directly (whether positively or negatively) to the on-load torque, which will be detailed in Section III.

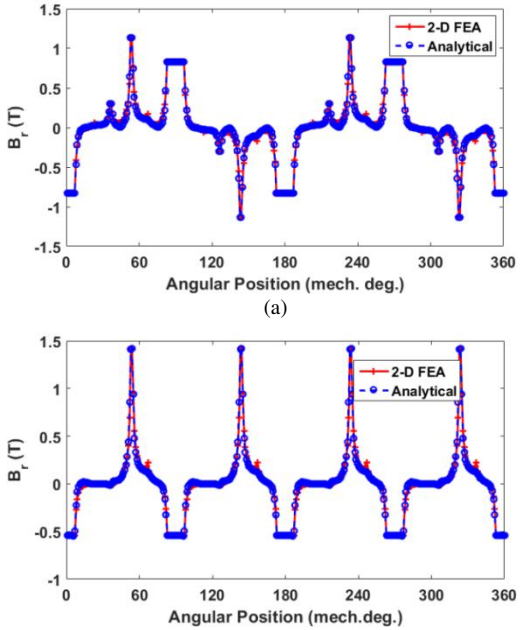

Fig. 15. Comparison of the 3-phase airgap flux density B_r between 2D FEA and analytical modelling at $10A_{rms}$. (a) DLC, and (b) DLMC.

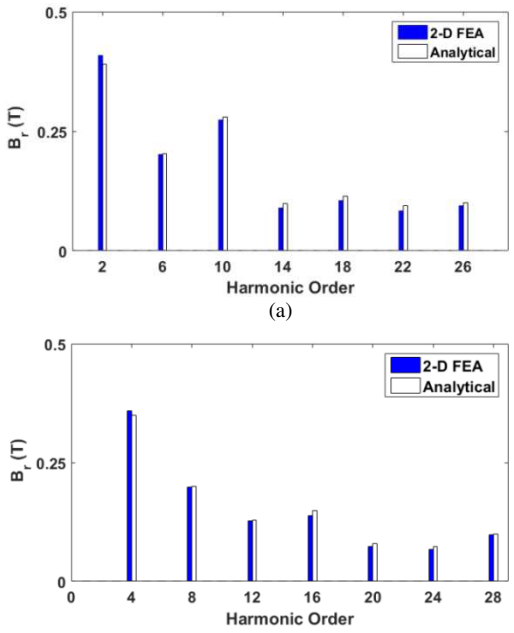

Fig. 16. Spectra of the 3-phase airgap flux density B_r between 2D FEA and analytical modelling at $10A_{rms}$. (a) DLC, and (b) DLMC.

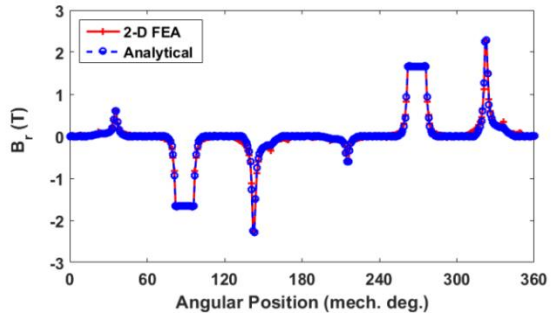

(a)

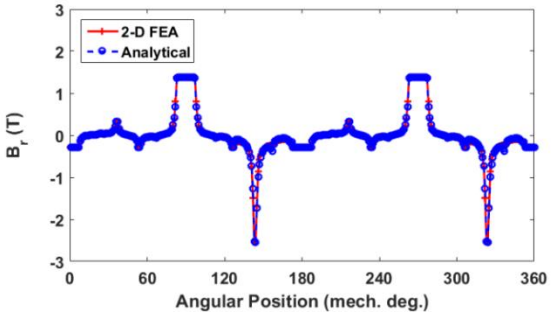

(b)

Fig. 17. Comparison of the 3-phase airgap flux density B_r between 2D FEA and analytical modelling at $10A_{rms}$. (a) SLC, and (b) SLMC.

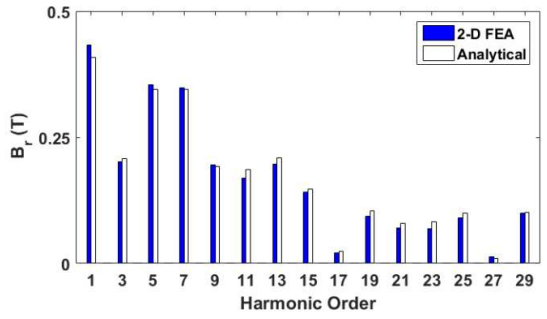

(a)

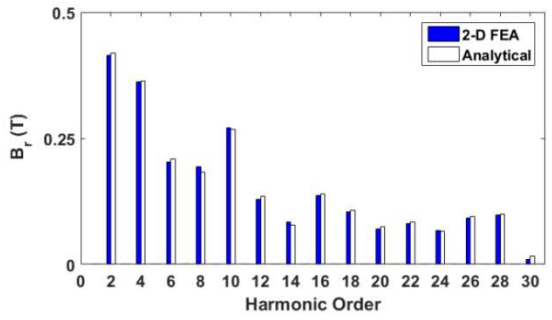

(b)

Fig. 18. Spectra of the 3-phase airgap flux density B_r between 2D FEA and analytical modelling at $10A_{rms}$. (a) SLC, and (b) SLMC.

IV. Contribution of Airgap Flux Density Harmonics to On-Load Torque

In this paper, the Maxwell stress tensor is used to investigate the contribution of the airgap flux density harmonics to on-load torque, which can be expressed as

$$T(t) = \frac{L}{\mu_0}\int_0^{2\pi} r^2 B_r B_t \, d\theta \tag{19}$$

where r is the airgap radius, L is the active length, and θ is the rotor position in mechanical degree. The radial and tangential airgap flux densities B_r and B_t can be expressed using Fourier series analysis as

$$\begin{cases} B_r(\theta,t) = \sum_i^{+\infty} B_{ri}\cos[i\theta - \theta_{ri}(t)] \\ B_t(\theta,t) = \sum_j^{+\infty} B_{tj}\cos[j\theta - \theta_{tj}(t)] \end{cases} \tag{20}$$

where B_{ri} and B_{tj} are the i^{th} and j^{th} order harmonics of B_r and B_t, respectively. In addition, θ_{ri} and θ_{tj} are the corresponding phases of each harmonic. Substituting (20) into (19), the instantaneous torque $T_{i,j}(t)$ generated by the i^{th} radial and j^{th} tangential airgap flux density harmonics can be given by

$$T_{i,j}(t) = \frac{Lr^2}{\mu_0}\int_0^{2\pi}\left\{\sum_i^{+\infty}\sum_j^{+\infty} B_{ri}B_{tj}\cos[i\theta - \theta_{ri}(t)]\cos[j\theta - \theta_{tj}(t)]\right\}d\theta \tag{21}$$

It is found that the instantaneous torque $T_{i,j}(t)$ can only be produced when $i = j$. It refers to the fact that only the same harmonic order of the radial and tangential airgap flux densities can contribute to the torque. It is worth mentioning that only the radial airgap flux density is calculated by analytical modelling in this paper, and the tangential airgap flux density is obtained by 2D FEA directly. Although the latter can also be calculated by analytical means such as subdomain methods in [15] or conformal mapping using complex airgap permeance model in [22], these methods are quite complicated to implement due to the doubly salient structure of the investigated machines and hence are not the main focus of this paper. Accordingly, the instantaneous torque can be rewritten as

$$T(t) = \sum_i^{+\infty} T_i(t) = \frac{\pi L r^2}{\mu_0}\sum_i^{+\infty} B_{ri}B_{ti}\cos[\theta_{ri}(t) - \theta_{ti}(t)] \tag{22}$$

Based on (22), the on-load torque can be obtained by summing the instantaneous torque $T_i(t)$. In addition, the positive or negative contribution to average torque can be calculated when instantaneous $T_i(t)$ and $T(t)$ are averaged. By way of example, $T_i(t)$ of the DLC and DLMC have been shown in Fig. 19, which account up to the 50th order harmonic in the airgap flux density. In addition, the resultant torque calculated by (22) has been compared to that obtained by direct 2D FEA and a good agreement can be observed.

In order to investigate the contribution of each harmonic in the airgap flux density to the on-load torque, the two most dominant harmonics in the radial airgap flux density (as shown in Fig. 16 and Fig. 18) have been selected. For example, the 2nd and 10th order harmonics are the two most dominant harmonics for the DLC as shown in Fig. 16, while the 4th and 16th order harmonics are selected for the DLMC. It is apparent in Fig. 19 that the 10th order harmonic in the airgap flux density of the DLC produces positive torque. However, the 2nd order harmonic produces negative torque. For the DLMC, the 4th and 8th order harmonics produce positive and negative torques, respectively. Similarly, the on-load torque produced by the two most dominant harmonics in the radial airgap flux density of the SLC and SLMC has been shown in Fig. 20 (a) and (b), respectively.

When looking at the rotating speed of the MMF shown in (8) and (10), the 10th order harmonic in the DLC and the 4th order harmonic in the DLMC have positive rotating speed. However, the 2nd order harmonic in the DLC and the 8th

order harmonic in the DLMC have negative rotating speed. As a result, it can be concluded that the dominant MMF harmonics with positive rotating speed (forward rotating) will produce positive torque. However, the dominant harmonics with backward rotating will produce negative torque. The dominant harmonic orders in MMF accounts for up to the 12^{th} order harmonics in both single and double layer machines. Also, it is worth mentioning that the dominant harmonics are the ones that contribute more than 5% of the resultant average torque.

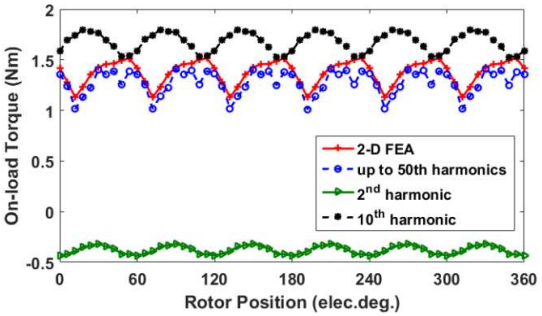

(a)

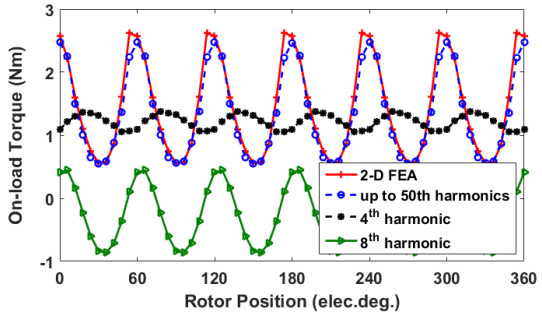

(b)

Fig. 19. Comparison of torques at $10A_{rms}$. (a) DLC, and (b) DLMC.

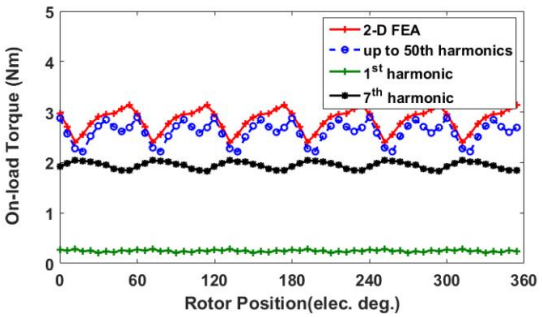

(a)

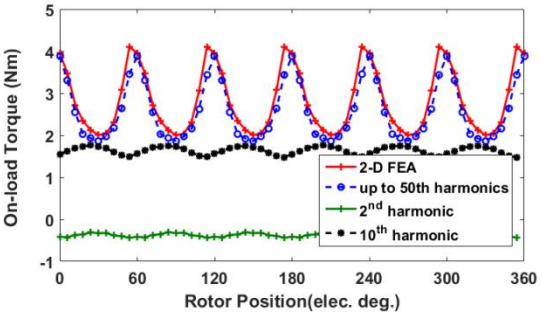

(b)

Fig. 20. Comparison of torques at $10A_{rms}$. (a) SLC, and (b) SLMC.

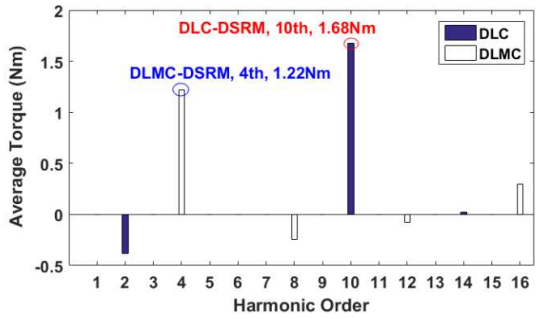

(a)

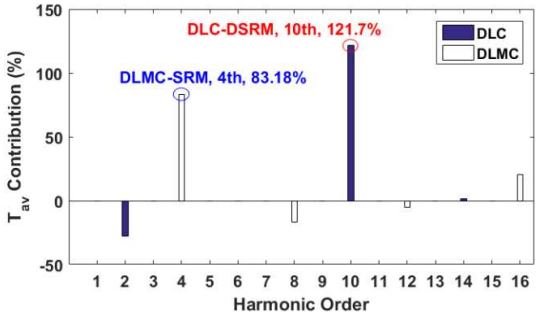

(b)

Fig. 21. (a) Average torque and (b) contribution to average torque by airgap flux density harmonics for the DLC and DLMC at $10A_{rms}$.

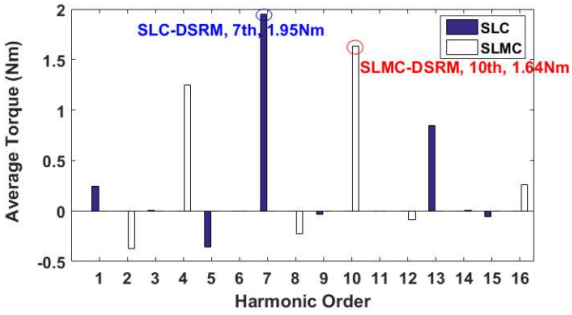

(a)

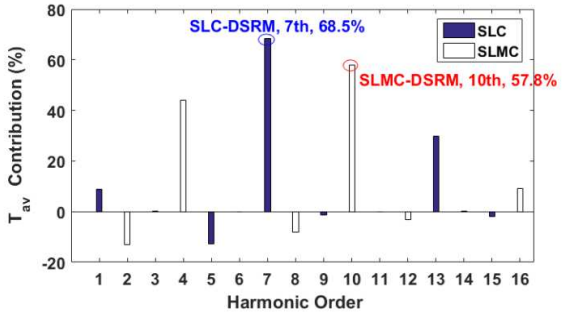

(b)

Fig. 22. (a) Average torque and (b) contribution to average torque by airgap flux density harmonics for the SLC and SLMC at $10A_{rms}$.

The instantaneous torque generated by the i^{th} order airgap flux density harmonics, where $i \leq 50$ has also been calculated. Moreover, the average torque produced by different airgap flux density harmonics of both the double and single layer DSRMs has been obtained as shown in Fig. 21 and Fig. 22, respectively. For clarity, the contribution of the airgap flux density harmonics to the average torque (>5%) and the torque ripple has been summarized in TABLE V.

In order to obtain the contribution of the i^{th} order harmonic to the torque ripple, the peak to peak value of resultant torque ($\Delta T_{result(without\ i^{th})}$) has been firstly calculated without the i^{th} order harmonic in the airgap field.

Then, the contribution of the i^{th} order harmonic to torque ripple can be given by

$$T_{rc} = \frac{\Delta T_{result} - \Delta T_{result(without\ i^{th})}}{\Delta T_{result}} \times 100\% \quad (23)$$

where ΔT_{result} is the difference between the maximum and minimum resultant torque.

It is found that the 10th order harmonic in the airgap flux density has the highest contribution (121.7%) to the average torque and contributes -45.73% to the torque ripple in the DLC. However, the 2nd order harmonic contributes -27.5% to the average torque. This means that the 10th order harmonic not only contributes to positive average torque but also has positive influence on the mitigation of the torque ripple. However, the 2nd order harmonic has negative influence on the average torque.

For the DLMC, the 4th order harmonic has the highest contribution (83.18%) to the average torque and while the 8th and 12th order harmonics generate negative average torque. For the single layer machines, the 7th order harmonic in the SLC has the highest contribution (68.5%) to the average torque while the 10th order harmonic in the SLMC contributes the most to the average torque (57.8%). Furthermore, it can be found that the harmonic order which has the most significant contribution to positive average torque can also reduce the resultant torque ripple, regardless of the winding configurations.

TABLE V CONTRIBUTION OF AIRGAP FIELD HARMONICS TO THE AVERAGE TORQUE AND THE TORQUE RIPPE

Winding configuration	Harmonic order	Contribution to average torque (%)	Contribution to torque ripple (%)
DLC-	2	-27.5	-3.02
	10	121.7	-45.73
DLMC-	4	83.2	-11.93
	8	-16.9	53.19
	12	-5.4	23.71
	16	20.2	0.24
	24	7.4	2.53
SLC-	1	8.7	2.16
	5	-12.6	-18.73
	7	68.5	-15.27
	13	29.7	-20.75
SLMC-	2	-13.2	-4.36
	4	44.1	-9.41
	8	-8.1	39.16
	10	57.8	-8.36
	16	9.12	0.78

V. CONCLUSION

By using simple analytical modeling for a 3-phase, 12-slot/8-pole doubly salient synchronous reluctance machines, this paper achieves a better understanding for the different torque production mechanisms between single/double layer, conventional/mutually-coupled winding configurations. According to the MMF model, it is found that the working harmonic orders of the mutually-coupled windings are doubled compared to the conventional windings. In addition, the harmonic orders of the double layer machines are also doubled compared to the single layer ones.

It is also found that the dominant MMF harmonics with positive (forward) rotating produce positive torque. However, the dominant harmonics with backward rotating produce negative torque. TABLE VI summarizes the harmonic orders in MMF_a and airgap flux density, as well as the dominant harmonics which contribute to positive (T_{AV}+) and negative (T_{AV}-) average torque. Based on the results, the future work would be the torque capability enhancement by reducing the MMF harmonics which contribute to negative torque through advanced control strategies such as harmonic current injection.

TABLE VI Summary of harmonic orders in MMF and airgap flux density, and their contribution to average torque

Winding configuration	MMF_a	Airgap flux density	$T_{AV}+$	$T_{AV}-$
DLC	4k-2	4k-2	10	2
DLMC	4k	4k	4	8
SLC	2k-1	2k-1	7	5
SLMC	2k	2k	10	2

VI. REFERENCES

[1] A. L. M. d. Santos, J. Anthonis, F. Naclerio, J. J. C. Gyselinck, H. V. d. Auweraer and L. C. S. Goes, "Multiphysics NVH modeling: simulation of a switched reluctance motor for an electric vehicle," *IEEE Trans. Ind. Electron.,* vol. 61, no. 1, pp. 469-476, Jan. 2014.

[2] T. J. E. Miller, "Optimal design of switched reluctance motors," *IEEE Trans. Ind. Electron.,* vol. 49, no. 1, pp. 15-27, Feb. 2002.

[3] D. E. Cameron, J. H. Lang and S. D. Umans, "The origin and reduction of acoustic noise in doubly salient variable-reluctance motors," *IEEE Trans. Ind. Appl.,* vol. 28, pp. 1250-1255, Nov./Dec. 1992..

[4] D. A. Torrey, X. M. Niu and E. J. Unkauf, "Analytical modelling of variable-reluctance machine magnetisation characteristics," *Proc. IEE—Elec. Power Appl.,* vol. 142, no. 1, pp. 14-22, Jan. 1995.

[5] S. A. Long, Z. Q. Zhu and D. Howe, "Effectiveness of active noise and vibration cancellation for switched reluctance machines operating under alternative control strategies," *IEEE Trans. Energy Convers.,* vol. 20, no. 4, pp. 792-801, Dec. 2005.

[6] D. A. Staton, W. L. Soong and T. J. E. Miler, "Unified theory of torque production in switched reluctance and synchronous reluctance motors," *IEEE Trans. Ind. Appl.,* vol. 31, no. 2, pp. 329-337, 1995.

[7] X. B. Liang., G. J. Li, J. Ojeda, M. Gabsi and Z. X. Ren, "Comparative study of classical and mutually coupled switched reluctance motors using multiphysics finite-element modeling," *IEEE Trans. Ind. Electron.,* vol. 61, no. 9, pp. 5066-5074, Oct. 2013.

[8] X. Ojeda, X. Mininger, M. Gabsi and M. Lecrivain, "Sinusoidal feeding for switched reluctance machine: application to vibration," in *Proc. ICEM*, Vilamoura, Portugal, Sep. 2008.

[9] G. J. Li, Z. Q. Zhu, X. Y. Ma and G. W. Jewell, "Comparative study of torque production in conventional and mutually coupled SRMs using frozen permeability," *IEEE Trans. Magn.,* vol. 52, no. 6, pp. 1-9, Jan. 2016.

[10] G. J. Li, J. Ojeda, E. Hoang, M. Lecrivain and M. Gabsi, "Comparative studies between classical and mutually coupled switched reluctance motors using thermal-electromagnetic analysis for driving cycles," *IEEE Trans. Magn.,* vol. 47, no. 4, pp. 839-847, Apr. 2011.

[11] J. W. Ahn, S. G. Oh, J. W. Moon and Y. M. Hwang, "A three-phase switched reluctance motor with two-phase excitation," *IEEE Trans. Ind. Appl.,* vol. 35, no. 5, pp. 1067-1075, Sep./Oct. 1999.

[12] J. W. Ahn, S. J. Park and D. H. Lee, "Hybrid excitation of SRM for reduction of vibration and acoustic noise," *IEEE Trans. Ind. Electron,* vol. 51, no. 2, pp. 374-380, Apr. 2004.

[13] X. Y. Ma, G. J. Li, G. W. Jewell, Z. Q. Zhu and H. L. Zhan, "Performance comparison of doubly salient reluctance machine topologies supplied by sinewave currents," *IEEE Trans. Ind. Electron.,* vol. 63, no. 7, pp. 4086-4096, Mar. 2016.

[14] Z. Q. Zhu and D. Howe, "Instantaneous magnetic field distribution in brushless permanent magnet dc motorss. III. effect of stator slotting," *IEEE Trans. Magn.,* vol. 29, no. 1, pp. 143-151, Jan. 1993.

[15] Z. Q. Zhu, L. Wu and Z. Xia, "An accurate subdomain model for magnetic field computation in slotted surface-mounted permanent-magnet," *IEEE Trans. Magn.,* vol. 47, no. 6, pp. 1100-1115, Apr. 2010.

[16] F. Dubas and C. Espanet, "Analytical solution of the magnetic field in permanent-magnet motors taking into account slotting effect: No-

load," *IEEE Trans. Magn.,* vol. 45, no. 5, pp. 2097-2109, May 2009.

[17] Z. Q. Zhu and D. Howe, "Instantaneous magnetic field distribution in brushless permanent dc motors. II. armature reaction field.," *IEEE Trans. Magn.,* vol. 29, no. 1, pp. 136-142, Jan. 1993.

[18] T. Lubin, T. Hamiti, H. Razik and A. Rezzoug, "Comparison between finite-element analysis and winding function theory for inductances and torque calculation of a synchronous reluctance machine," *IEEE Trans. Magn.,* vol. 43, no. 8, pp. 3406-3410, Aug. 2007.

[19] G. Dajaku and D. Gerling, "Stator slotting effect on the magnetic field distribution of salient pole synchronous permanent-magnet machines," *IEEE Trans. Magn.,* vol. 46, no. 9, pp. 3676-3683, Sep. 2010.

[20] B. Gaussens, E. Hoang, O. d. l. Barriere, J. S. Michel, M. Lecrivain and M. Gabsi, "Analytical approach for air-gap modeling of field-excited flux-switching machine: no-load operation," *IEEE Trans. Magn.,* vol. 48, no. 9, pp. 2505-2517, Sep. 2012.

[21] B. Gaussens, E. Hoang, O. d. l. Barriere, J. S. Michel, P. Manfe, M. Lecrivain and M. Gabsi, "Analytical armature reaction field prediction in field-excited flux-switching machines using an exact relative permeance function," *IEEE Trans. Magn.,* vol. 49, no. 1, pp. 628-641, Aug. 2012.

[22] D. Zarko, D. Ban and T. A. Lipo, "Analytical calculation of magnetic field distribution in the slotted air gap of a surface permanent-magnet motor using complex relative air-gap permeance," *IEEE Trans. Magn.,* vol. 42, no. 7, pp. 1828-1837, Jun. 2006.